Disordered transition metal dichalcogenides: A coherent potential approximation study

Pedro L. Alcázar Ruano,[1,2] Dunkan Martínez,[1] Olga Arroyo-Gascón,[3] Yuriko Baba,[4] Jorge Quereda,[2] and Francisco Domínguez-Adame[1]

[1]*GISC, Departamento de Física de Materiales, Universidad Complutense, E-28040 Madrid, Spain*

[2]*2D Foundry Group. Instituto de Ciencia de Materiales de Madrid (ICMM-CSIC), E-28049 Madrid, Spain*

[3]*Nanotechnology Group, USAL – Nanolab, Departamento de Física Fundamental, Universidad de Salamanca, E-37008 Salamanca, Spain*

[4]*Departamento de Física Teórica de la Materia Condensada, Universidad Autónoma de Madrid, E-28049 Madrid, Spain*

(Received 15 June 2025; revised 24 July 2025; accepted 28 July 2025; published 8 August 2025)

We introduce a solvable four-band model to study electron energy levels in disordered transition metal dichalcogenides. Electron states in the pristine monolayer are described by a $\boldsymbol{k}\cdot\boldsymbol{p}$ Hamiltonian. Point defects are assumed to be randomly distributed on a regular lattice. The interaction of electrons with the defects is accounted for by a separable pseudopotential, thus yielding a solvable model suitable for long- and short-range interactions. The coherent potential approximation is used to obtain the configurationally averaged density of states. We compare to models of disorder, namely, binary disorder and Anderson disorder. Importantly, both disorder models yield consistent outcomes, demonstrating that an increase in disorder strength results in a narrowing of the energy gap. Remarkably, CPA with binary disorder provides results that are in very good agreement with available density functional theory and experimental data for the optical gap in the monolayer alloy $Mo_{1-x}W_xS_2$. Moreover, it entails less computational effort than density functional theory calculations.

DOI: 10.1103/58pr-k9vt

I. INTRODUCTION

Layered transition metal dichalcogenides (TMDs) constitute a class of materials that can be exfoliated into monolayers, displaying specific physical properties not shared by their bulk counterpart [1,2]. Their chemical formula is MX_2, where M is a transition metal (usually molybdenum, tungsten, or rhenium) and X is a chalcogen other than oxygen (sulfur, selenium, tellurium). The crossover from an indirect-gap semiconductor at multilayers to a direct band-gap one at monolayer as well as high electron mobility make TMDs materials of choice for optoelectronic applications. Electron states near the valence band maximum and the conduction band minimum are mainly composed of the d orbitals of the metal atom and p orbitals of the chalcogen atom, respectively. Most common monolayer TMDs present an optical band gap of about $1.6-2.0\,\mathrm{eV}$, paving the way for the design of optical devices, such as photodetectors [3], in the visible range.

Crystalline defects have a more pronounced impact on the physical properties of monolayer TMDs compared to their multilayer structures because of their reduced dimensionality. Point defects (PDs), such as impurities, vacancies and interstitials, play a critical role in tailoring the electronic and optical properties of these materials [4,5]. Disorder induced by a significant amount of PDs creates a random potential landscape that inhomogeneously broadens electron levels of TMDs, as revealed by optical techniques [6–8]. The interplay between disorder and electron-electron interactions is responsible for the enhancement by an order of magnitude of the transition temperature for Wigner crystallization compared to pristine TMDs [9].

The density of states (DOS) plays a central role in determining the physical behavior of TMDs. PDs can significantly alter the DOS, introducing localized states in the band gap and perturbing the states near the band edges. For instance, sulfur vacancies are particularly common in MoS_2 due to the lower formation energy and play a dominant role in modifying the DOS [10–12]. A sulfur vacancy introduces defect states within the band gap, which can act as trap states or recombination centers [13].

From a theoretical viewpoint, *ab initio* approaches, such as density functional theory (DFT), are extensively utilized for calculating the electronic structure and the DOS in disordered TMDs [14–17]. These methods provide accurate ground-state properties but are computationally intensive, thereby limiting their application to relatively small supercells. In contrast, tight-binding approaches [18–21] and $\boldsymbol{k}\cdot\boldsymbol{p}$ models [22–24] are well suited for large-scale simulations and for capturing qualitative features of the DOS. However, their parameters typically require fitting against DFT calculations or experimental measurements.

The coherent potential approximation (CPA) is a well-established theoretical method used to describe electron and phonon states in disordered materials [25–27]. The CPA, originally rooted in Lax's work on wave scattering in effective media [28], was proposed by Soven [29] and later refined by Velický *et al.* [30] for tight-binding electrons and by Taylor [31] for phonons in the late 1960s. The formulation of the CPA within the multiple scattering framework, specifically the Korringa-Kohn-Rostoker method, was developed by Shiba [32] (see also Ref. [33] and references therein). The CPA provides a way to study quasiparticle states (electrons, phonons, excitons, magnons) in disordered systems by replacing the random potential with an effective (coherent), translationally invariant potential. This approach allows for the self-consistent calculation of physical quantities like

TABLE I. Model parameters for monolayer TMDs reported in Ref. [22]

	Δ (eV)	$\hbar$v (eV Å)	α (eV)
MoS_2	0.830	3.51	0.0375
WS_2	0.895	4.38	0.1075
$MoSe_2$	0.735	3.11	0.0450
WSe_2	0.800	3.94	0.1150

the DOS, conductivity, and magnetic properties, even in the strong disorder limit. The CPA yields a much more accurate description of substitutional disorder than simpler approaches like the virtual crystal approximation (VCA), as discussed below. Compared to full-scale DFT calculations, the CPA is notably less computationally demanding, making it useful for studying a wide range of concentrations of PDs and models of disorder. In this work, we explore the impact of defects on the DOS by extending the CPA to disordered TMDs. To this end, we start from a $\boldsymbol{k}\cdot\boldsymbol{p}$ Hamiltonian to describe the defect-free material and replace the electron-defect interaction potential with a separable pseudopotential. In this way, we obtain a model that is exactly solvable for calculating the coherent potential describing the effective medium. Two models of disorder due to the presence of PDs will be studied, namely, binary disorder and Anderson disorder [34]. Although both models of disorder lead to qualitatively similar results, when compared with experiments we find that the binary disorder model is more realistic for describing TMDs with a random distribution of PDs.

II. THEORETICAL MODEL

In most common monolayer TMDs (MoS_2, $MoSe_2$, WS_2 and WSe_2), *ab initio* calculations indicate that the conduction- and valence-band edges are located at the two nonequivalent valleys K and K' of the hexagonal Brillouin zone [35,36]. The enhanced spin-orbit coupling induces a large spin splitting of the valence band, while the conduction band remains degenerated. The minimal band model obtained by general symmetry considerations yields the following two-band $\boldsymbol{k}\cdot\boldsymbol{p}$ Hamiltonian up to first order in the in-plane momentum [22]:

$$\widehat{H}_0 = s_0 \otimes (\hbar \mathrm{v}\boldsymbol{\sigma}\cdot\widehat{\boldsymbol{k}} + \Delta\sigma_z) + \alpha\tau s_z \otimes (\sigma_z - \sigma_0), \qquad (1)$$

in the basis $|\,\phi_c\,\rangle = |\,d_{z^2}\,\rangle$ and $|\,\phi_v^\tau\,\rangle = (1/\sqrt{2})(|\,d_{x^2-y^2}\,\rangle - \mathrm{i}\,\tau|\,d_{xy}\,\rangle)$, where $\tau = \pm 1$ is the valley index and the subscripts c and v refer to the conduction band and valence band, respectively. Here $\widehat{\boldsymbol{k}}$ is the in-plane momentum operator, and σ_j $(j = x, y, z)$ and σ_0 denote the Pauli matrices and the 2×2 unit matrix acting upon the basis functions. Similarly, s_z and s_0 are the Pauli matrix and the 2×2 unit matrix for spin. Since both matrices s_z and s_0 are diagonal, spin-up and spin-down components are decoupled in this basis. In Eq. (1), v is a model parameter with dimensions of velocity, 2Δ is the energy gap and 4α is the valence-band splitting caused by the spin-orbit coupling. These parameters are obtained by fitting *ab initio* band structure calculations [22] and are presented in Table I.

For the sake of concreteness, we will restrict ourselves to a single valley hereafter. The Hamiltonian $\widehat{H}_0$ given by (1) with $\tau = 1$ turns out to be block diagonal,

$$\widehat{H}_0 = \begin{pmatrix} \widehat{H}_+ & 0 \\ 0 & \widehat{H}_- \end{pmatrix}, \qquad (2a)$$

with

$$\widehat{H}_\pm = \hbar \mathrm{v}\boldsymbol{\sigma}\cdot\widehat{\boldsymbol{k}} + (\Delta \pm \alpha)\sigma_z \mp \alpha\sigma_0. \qquad (2b)$$

Besides the trivial energy shift $\mp\alpha$ given by the last term, each block $\widehat{H}_\pm$ corresponds to a two-dimensional massive Dirac Hamiltonian with a spin-dependent gap $\Delta \pm \alpha$.

In disordered TMDs, the single electron Hamiltonian splits as $\widehat{H} = \widehat{H}_0 + \widehat{H}_{\mathrm{dis}}$, where the translationally invariant part is given by Eq. (1). $\widehat{H}_{\mathrm{dis}}$ takes into account the electron interaction with a random distribution of PDs. To proceed, we will assume that PDs are located at random on a regular square lattice of parameter a. It is most important to stress that a is not related to the size of the unit cell of the honeycomb, hexagonal lattice of TMDs. In fact, electrons do not *see* the crystal structure since we are using a $\boldsymbol{k}\cdot\boldsymbol{p}$ approximation for the Hamiltonian (1) for the pristine sample. The actual electron interaction potential with the random array of PDs will be replaced by the following separable pseudopotential [37–40]:

$$\widehat{H}_{\mathrm{dis}} = \sum_n |\,\omega_n\,\rangle\lambda_n\langle\,\omega_n\,|, \qquad (3)$$

where n runs over all sites $\boldsymbol{R}_n$ of the square lattice and $\omega(\boldsymbol{r}-\boldsymbol{R}_n) = \langle\,\boldsymbol{r}\,|\,\omega_n\,\rangle$ will be referred to as the shape function. λ_n is the coupling constant that takes random values with a given probability distribution. We neglect valley and spin mixing and assume that λ_n is a scalar. In spite of its seemingly more complicated form, the separable pseudopotential model is amenable to analytical solution for any arbitrary shape function and allows us to obtain closed expressions for the DOS within the CPA framework [37].

Two different models of disorder will be addressed in this work. First, we will focus on binary disorder, when two different species of PDs are considered. A given site of the square lattice is occupied by a defect A with probability c or by a defect B with probability $1-c$. Hence, the probability distribution in this model of binary disorder is

$$\mathcal{P}(\lambda_n) = c\delta(\lambda_n - \lambda_{\mathrm{A}}) + (1-c)\delta(\lambda_n - \lambda_{\mathrm{B}}). \qquad (4a)$$

Second, we will also deal with Anderson disorder [34] with a top hat probability distribution of width W,

$$\mathcal{P}(\lambda_n) = \frac{1}{W}\,\theta(W/2 - |\overline{\lambda} - \lambda_n|), \qquad (4b)$$

where θ is the Heaviside step function and $\overline{\lambda} > W/2$, so $\lambda_n > 0$. Averages over the probability distributions (4) will be denoted as $\langle\cdots\rangle_{\mathrm{av}}$ hereafter.

III. COHERENT POTENTIAL APPROXIMATION

In the body of the paper, we will be concerned with the generalization of the CPA to TMDs. Among other well-established approaches, the CPA is an excellent and accurate alternative to purely numerical calculations. The starting point

is the retarded resolvent of the Hamiltonian $\widehat{H}$, formally defined as [26,27]

$$\widehat{G}(z) \equiv \frac{1}{z-\widehat{H}}, \quad z \equiv E + \mathrm{i}\,0^{+}. \tag{5}$$

The use of the exact resolvent is impractical because it incorporates the random potential given in Eq. (3). For this reason, our interest concerns its average over the possible configurations of the disorder

$$\langle \widehat{G}(z) \rangle_{\mathrm{av}} = \int \mathcal{P}(\lambda_n) \widehat{G}(z) \mathrm{d}\lambda_n, \tag{6}$$

from which the average DOS can be readily obtained. According to the single-site CPA, the average resolvent is calculated by introducing a periodic (translationally invariant) effective medium characterized by a single coupling constant λ. On the other hand, this effective coupling constant is determined by replacing λ by λ_n at an arbitrary site n of the effective medium and imposing that the scattering off on average equals that of the effective medium itself [26].

The effective medium will be described by a Hamiltonian $\widehat{H}_{\mathrm{M}}$ that is to be determined. By definition, the corresponding resolvent is $\widehat{G}_{\mathrm{M}}(z) = 1/(z - \widehat{H}_{\mathrm{M}})$, where $\widehat{H}_{\mathrm{M}}$ is assumed to be cast in the form [37]

$$\widehat{H}_{\mathrm{M}} = \widehat{H}_0 + \sum_n |\omega_n\rangle \lambda \langle \omega_n|. \tag{7}$$

Notice that, in the general case, the effective coupling constant λ will be a 4×4 complex matrix such that $\widehat{G}_{\mathrm{M}}(z) = \langle \widehat{G}(z) \rangle_{\mathrm{av}}$. From Eq. (5), one can write

$$\widehat{G}(z) = \frac{1}{z - \widehat{H}_{\mathrm{M}} - \widehat{V}} = \frac{\widehat{G}_{\mathrm{M}}(z)}{1 - \widehat{V}\,\widehat{G}_{\mathrm{M}}(z)}, \tag{8a}$$

where we have defined

$$\widehat{V} = \sum_n |\omega_n\rangle (\lambda_n - \lambda) \langle \omega_n| \equiv \sum_n \widehat{V}_n. \tag{8b}$$

Now we define the scattering operator $\widehat{T}$ through its relation with the resolvents as follows [26]:

$$\widehat{G}(z) = \widehat{G}_{\mathrm{M}}(z)[1 + \widehat{T}(z)\,\widehat{G}_{\mathrm{M}}(z)], \tag{9a}$$

which, when compared with Eq. (8a), leads to

$$\widehat{T}(z) = [1 - \widehat{V}\,\widehat{G}_{\mathrm{M}}(z)]^{-1} \widehat{V}. \tag{9b}$$

Once we take the configuration average of Eq. (9a), and bearing in mind that $\widehat{G}_{\mathrm{M}}(z)$ describes a periodic (nonrandom) medium, we obtain that the condition $\widehat{G}_{\mathrm{M}}(z) = \langle \widehat{G}(z) \rangle_{\mathrm{av}}$ leads to

$$\langle \widehat{T}(z) \rangle_{\mathrm{av}} = 0. \tag{10}$$

Equation (10) can be viewed as an implicit equation for the determination of the coupling constant λ of the effective medium because it enters the expression of $\widehat{V}$ given by Eq. (8b). However, from Eq. (11) it is apparent that the calculation of the configuration average is complicated. In fact, $\widehat{V}$ is a summation that runs over all lattice sites. The CPA makes a step forward and replaces $\widehat{V}$ by a single-site potential $\widehat{V}_n$ in Eq. (10), which amounts to neglecting multiple scattering events as a first-order approximation. Therefore, the central equation of the CPA reads

$$\left\langle \left[1 - \widehat{V}_n\,\widehat{G}_{\mathrm{M}}(z)\right]^{-1} \widehat{V}_n \right\rangle_{\mathrm{av}} = 0. \tag{11}$$

The expansion $(1-x)^{-1} = \sum_{\ell=0}^{\infty} x^{\ell}$ and the definition $\widehat{V}_n = |\omega_n\rangle(\lambda_n - \lambda)\langle\omega_n|$ given in Eq. (8b) lead to

$$\begin{aligned} &\left[1 - \widehat{V}_n\,\widehat{G}_{\mathrm{M}}(z)\right]^{-1} \widehat{V}_n \\ &\quad = |\omega_n\rangle \left[1 - (\lambda_n - \lambda) F(z,\lambda)\right]^{-1} (\lambda_n - \lambda) \langle \omega_n| \,, \end{aligned} \tag{12a}$$

with (see Appendix A and Ref. [40] for further details)

$$\begin{aligned} F(z,\lambda) &= \langle \omega_n | \widehat{G}_{\mathrm{M}}(z) | \omega_n \rangle \\ &= \int |\omega(\boldsymbol{k})|^2 \mathcal{D}(z,\lambda,\boldsymbol{k})\, \mathrm{d}^2\boldsymbol{k} \end{aligned} \tag{12b}$$

and

$$\mathcal{D}(z,\lambda,\boldsymbol{k}) = \left(z - \frac{4\pi^2}{a^2} \lambda |\,\omega(\boldsymbol{k})|^2 - H_0(\boldsymbol{k}) \right)^{-1}. \tag{12c}$$

Here we take into account that the Hamiltonian $\widehat{H}_0$ is diagonal in the plane wave basis and write $H_0(\boldsymbol{k}) = \langle \boldsymbol{k}|\widehat{H}_0|\boldsymbol{k}\rangle$. $\omega(\boldsymbol{k}) = (1/2\pi) \int \exp(\mathrm{i}\,\boldsymbol{k}\cdot\boldsymbol{r}) \omega(\boldsymbol{r})\, \mathrm{d}^2\boldsymbol{r}$ is the Fourier transform of the shape function that we assumed to vanish outside the first Brillouin zone [37]. Therefore, Eq. (11) yields

$$\left\langle \frac{\lambda_n - \lambda}{1 - (\lambda_n - \lambda) F(z,\lambda)} \right\rangle_{\mathrm{av}} = 0. \tag{12d}$$

The knowledge of $\langle \widehat{G}(z) \rangle_{\mathrm{av}} = \widehat{G}_{\mathrm{M}}(z)$ allows us to obtain the configurationally averaged spectral properties of the electron states in disordered TMDs. In particular, the average DOS per unit area is computed from the following expression:

$$\begin{aligned} \rho(E) &= -\frac{1}{\pi S} \mathrm{Im}\left[\mathrm{Tr}\left(\widehat{G}_{\mathrm{M}}(E + \mathrm{i}\,0^{+})\right)\right] \\ &= -\frac{1}{4\pi^3} \mathrm{Im}\left[\mathrm{Tr} \int \mathcal{D}(E + \mathrm{i}\,0^{+}, \lambda, \boldsymbol{k})\, \mathrm{d}^2\boldsymbol{k} \right], \end{aligned} \tag{13}$$

where S is the area of the TMD.

IV. RESULTS

Note that our approach is valid for any arbitrary function $\omega(\boldsymbol{k})$. Therefore, it is suitable for the study of short-range and long-range interaction potentials. In this paper, we will focus on short-range shape functions and assume that $\omega(\boldsymbol{k})$ is spherically symmetric. We will take

$$\omega(\boldsymbol{k}) = \omega(k) = \frac{a}{2\pi}\, \theta(k_c - k), \tag{14}$$

where θ is the Heaviside step function and k_c is a momentum cutoff to ensure that $\omega(\boldsymbol{k})$ vanishes outside the first Brillouin zone. It is straightforward to demonstrate that the off-diagonal terms of the 4×4 matrix appearing in the integrand of Eq. (12b) are odd functions of $\boldsymbol{k}$ and vanish after integration. Therefore, we can write the coupling constant of the effective medium as a block-diagonal matrix $\lambda = \mathrm{diag}(\lambda_0^{+}\sigma_0 + \lambda_z^{+}\sigma_z, \lambda_0^{-}\sigma_0 + \lambda_z^{-}\sigma_z)$ and

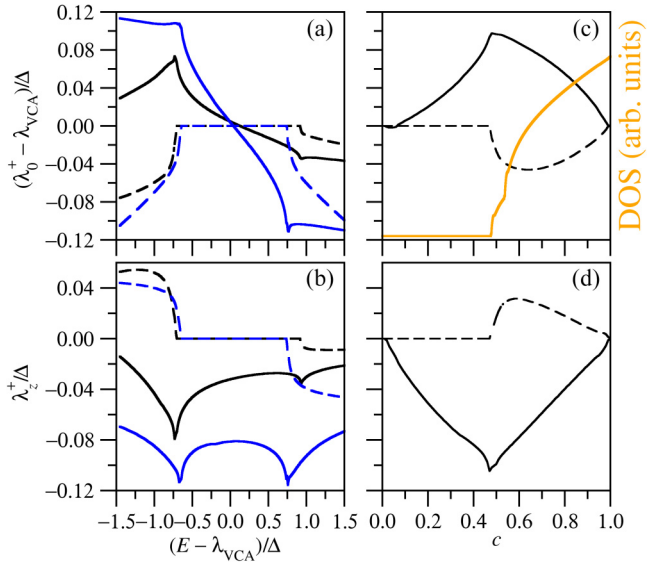

FIG. 1. Real (solid lines) and imaginary (dashed lines) of the effective coupling constants (a) λ_0^+ and (b) λ_z^+ as a function of the shifted energy $E - \lambda_{VCA}$ for $c = 0.1$ (black lines) and $c = 0.5$ (blue lines), when $\lambda_A = 1.5\Delta$ and $\lambda_B = 0$. Real (solid lines) and imaginary (dashed lines) of the effective coupling constants (c) λ_0^+ and (d) λ_z^+ as a function of the fraction of PDs at $E = 0$. The effective coupling constant obtained within the virtual crystal approximation $\lambda_{VCA} = c\lambda_A$ has been subtracted in panels (a) and (b) for convenience. Orange solid line in panel (c) shows the corresponding average DOS at $E = 0$ in arbitrary units.

$F(z, \lambda) = \mathrm{diag}[F_+(z, \lambda_0^+, \lambda_z^+), F_-(z, \lambda_0^-, \lambda_z^-)]$ turns out to be a block-diagonal matrix as well, where

$$F_\pm(z, \lambda_0^\pm, \lambda_z^\pm) = \frac{a^2}{2\pi}\,[(z \pm \alpha - \lambda_0^\pm)\sigma_0 + (\Delta \pm \alpha - \lambda_z^\pm)\sigma_z]J_\pm(z, \lambda_0^\pm, \lambda_z^\pm), \quad (15a)$$

with

$$J_\pm(z, \lambda_0^\pm, \lambda_z^\pm) = \int_0^{k_c} [(z \pm \alpha - \lambda_0^\pm)^2 - (\Delta \pm \alpha - \lambda_z^\pm)^2 - \hbar^2 v^2 k^2]^{-1} k\, \mathrm{d}k. \quad (15b)$$

After the scalar functions $\lambda_0^\pm(E)$ and $\lambda_z^\pm(E)$ have been obtained by solving Eq. (12d), the average DOS per unit area is calculated as $\rho(E) = \rho_+(E) + \rho_-(E)$, where

$$\rho_\pm(E) = -\frac{1}{\pi^2}\,\mathrm{Im}[(E \pm \alpha - \lambda_0^\pm)J_\pm(z, \lambda_0^\pm, \lambda_z^\pm)]. \quad (16)$$

We set $a = 0.3\,\mathrm{nm}$ and $k_c a = \pi$ in what follows. Concerning the material parameters, as a working example we take $(\hbar v/a\Delta)^2 = 2$ and $\alpha = 0.0452\Delta$, corresponding to MoS_2 (see Table I). However, other TMDs exhibit comparable ratios, and therefore our general conclusions remain valid.

A. Binary disorder

Figures 1(a) and 1(b) show the real and the imaginary parts of the effective coupling constants λ_0^+ and λ_z^+ in the case of random binary disorder (4a) when $\lambda_A = 1.5\Delta$ and $\lambda_B = 0$ and for two different values of the fraction of PDs, $c = 0.1$ and $c = 0.5$. Similar results are obtained for λ_0^- and λ_z^- and will be not shown. For convenience, $\lambda_0^+ - \lambda_{VCA}$ is plotted, where $\lambda_{VCA} = \langle\lambda_n\rangle_{av} = c\lambda_A + (1-c)\lambda_B$ is the effective coupling constant obtained within the virtual crystal approximation. Notice that λ_{VCA} is real, so only the real part of λ_0^+ is shifted. From Fig. 1(a), we observe that $\mathrm{Re}(\lambda_0^+)$ is larger (smaller) than λ_{VCA} when E is above (below) λ_{VCA} while $\mathrm{Re}(\lambda_z^+)$ is negative over the whole energy range. The gap determined from the vanishing of $\mathrm{Im}(\lambda_0^+)$ is roughly symmetric with respect to $E = \lambda_{VCA}$ and shrinks on increasing the fraction of PDs up to $c = 0.5$. It is worth stressing that $\mathrm{Im}(\lambda_0^+\sigma_0 + \lambda_z^+\sigma_z)$ is negative, as expected. Figures 1(c) and 1(d) show the real and the imaginary parts of the effective coupling constants λ_0^+ and λ_z^+ at $E = 0$ as a function of the fraction of PDs for the same values of λ_A and $\lambda_B = 0$. We observe that the deviation of λ_0^+ from the VCA prediction is more apparent at $c = 0.476$, namely, when disorder is close to maximal. As shown in Fig. 1(c), the corresponding average DOS (in arbitrary units) reveals that the maximal deviation arises when the band edge is located at $E = 0$.

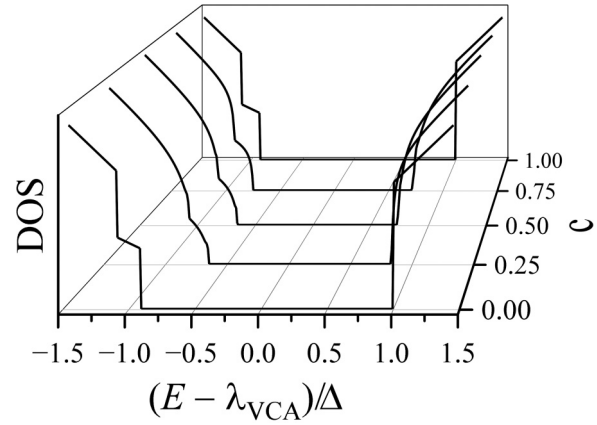

FIG. 2. Average density of states in arbitrary units for binary disorder as a function of the shifted energy $E - \lambda_{VCA}$ and the fraction of PDs when $\lambda_A = 1.5\Delta$ and $\lambda_B = 0$.

After discussing the salient features of the coupling constant of the effective medium, we turn our attention to the average DOS. Figure 2 shows the average DOS $\rho(E)$ as a function of $E - \lambda_{VCA}$ when $\lambda_A = 1.5\Delta$ and $\lambda_B = 0$, and for several values of the fraction of PDs. We observe that in the limiting cases $c = 0$ and $c = 1$, namely, when the system is ordered, the DOS remains the same when plotted as a function of the shifted energy $E - \lambda_{VCA}$. In all other cases, the DOS smooths out near the band edges and the gap becomes narrower compared with the ordered TMD.

B. Anderson disorder

Figures 3(a) and 3(b) show the real and the imaginary parts of the effective coupling constants λ_0^+ and λ_z^+ in the case of Anderson disorder (4b) when $\bar{\lambda} = \Delta$ and for two different values of the magnitude of disorder, $W = 2\Delta/3$ and $W = \Delta$. As in the previous section, $\lambda_0^+ - \lambda_{VCA}$ is plotted, where now $\lambda_{VCA} = \langle\lambda_n\rangle_{av} = \bar{\lambda}$. From Fig. 3, we observe that $\mathrm{Re}(\lambda_0^+)$ and $\mathrm{Im}(\lambda_0^+)$ are odd and even functions of the shifted energy $E - \lambda_{VCA}$, respectively. On the contrary, $\mathrm{Re}(\lambda_z^+)$ and $\mathrm{Im}(\lambda_z^+)$

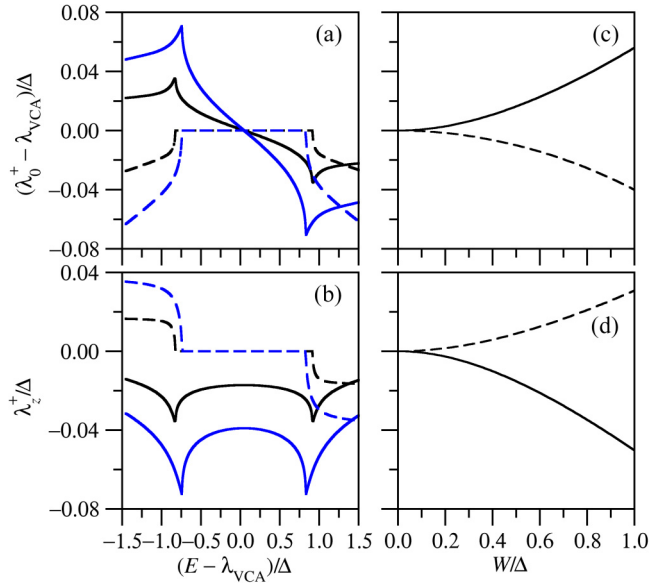

FIG. 3. Real (solid lines) and imaginary (dashed lines) of the effective coupling constants (a) λ_0^+ and (b) λ_z^+ as a function of the shifted energy $E - \lambda_{VCA}$ for $W = 2\Delta/3$ (black lines) and $W = \Delta$ (blue lines), when $\overline{\lambda} = \Delta$. Real (solid lines) and imaginary (dashed lines) of the effective coupling constants (c) λ_0^+ and (d) λ_z^+ as a function of the magnitude of disorder at $E = 0$, when $\overline{\lambda} = \Delta$. The effective coupling constant obtained within the virtual crystal approximation $\lambda_{VCA} = \overline{\lambda}$ has been subtracted in panels (a) and (c) for convenience.

are even and odd functions of the shifted energy, respectively. The gap shrinks on increasing the magnitude of disorder W. As in the binary disorder model, $\mathrm{Im}(\lambda_0^+\sigma_0 + \lambda_z^+\sigma_z)$ is negative (not shown in the figure). Figures 3(c) and 3(d) show the real and the imaginary parts of the effective coupling constants λ_0^+ and λ_z^+ at $E = 0$ in the case of Anderson disorder (4b) when $\overline{\lambda} = \Delta$, as a function of the magnitude of disorder W. We observe that the deviation of λ_0^+ from the VCA prediction is more apparent on increasing W. Figure 4 shows the average DOS $\rho(E)$ a function of $E - \lambda_{VCA}$ when $\overline{\lambda} = \Delta$ and for several values of the magnitude of disorder. We observe that the DOS becomes smoother near the band edges, and the

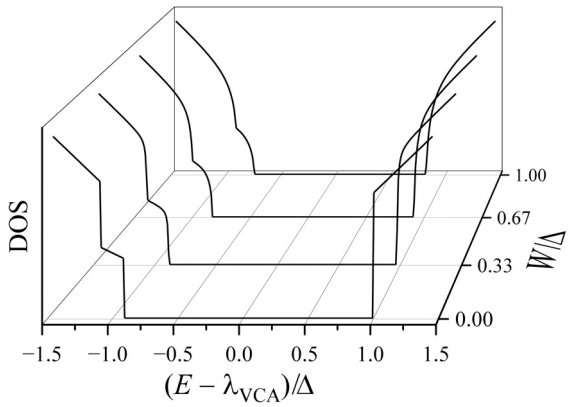

FIG. 4. Average density of states in arbitrary units as a function of shifted energy $E - \lambda_{VCA}$ and the magnitude of Anderson disorder when $\overline{\lambda} = \Delta$.

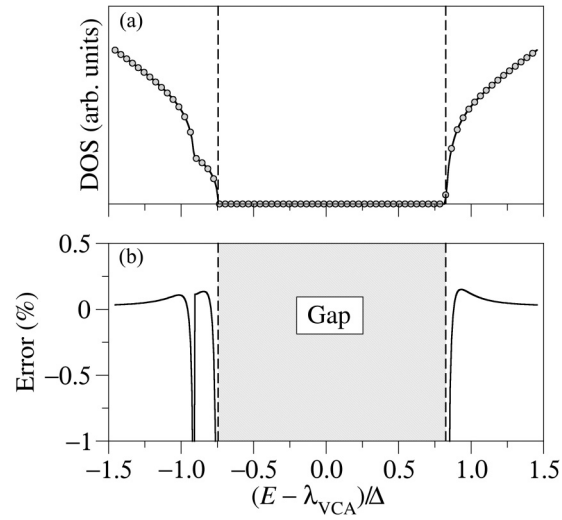

FIG. 5. (a) Average density of states from in arbitrary units as a function of the shifted energy $E - \lambda_{VCA}$ when $\overline{\lambda} = W = \Delta$. Circles and solid line correspond to the approximation given by Eq. (18) and the exact result, respectively. (b) Error defined in the main text as a function of the shifted energy, demonstrating the remarkable accuracy of the approximation except at energies very close to the three band edges. Shadowed area indicates the band gap.

energy gap narrows as the magnitude of disorder increases, in agreement with observations in the case of binary disorder.

If Anderson disorder is weak ($W \to 0$), calculations can be largely simplified. To this end, we start from the configurational average (12d) with the probability distribution (4b). Recalling that both λ and $F(z, \lambda)$ are diagonal matrices, we get

$$F(z,\lambda) = \frac{1}{W}\,\ln\left[\frac{1 + (\lambda - \overline{\lambda} + W/2)F(z,\lambda)}{1 + (\lambda - \overline{\lambda} - W/2)F(z,\lambda)}\right]. \qquad (17)$$

Expanding the right-hand side up to second order in W and assuming that the elements of the matrix $(\lambda - \overline{\lambda})F(z, \lambda)$ are smaller than unity, we arrive at

$$\lambda = \overline{\lambda} + \frac{W^2}{12}\,F(z,\lambda) \simeq \overline{\lambda} + \frac{W^2}{12}\,F(z,\overline{\lambda}). \qquad (18)$$

Therefore, in the limit of weak Anderson disorder we get an explicit equation for the coupling constant of the effective medium $\lambda(z)$ in terms of $\overline{\lambda}$ and $W/2$. Figure 5(a) presents a comparison between the exact DOS and the DOS obtained from the approximate coupling constant (18) when $\overline{\lambda} = W = \Delta$. Although the magnitude of the Anderson disorder cannot be regarded as small, the agreement is excellent. The error, used to assess the accuracy of the approximation, is defined as follows: $100 \times (\rho_{exact} - \rho_{approx})/(\rho_{exact} + \rho_{approx})$. Figure 5(b) presents the error as a function of the shifted energy, demonstrating the accuracy of Eq. (18) except at energies very close to the three band edges.

V. COMPARISON WITH EXPERIMENT

Finally, a comparison is made between the predictions of the CPA and the DFT results reported in Ref. [41]. In that

study, the evolution of the optical energy gap in the monolayer alloy $Mo_{1-x}W_xS_2$ was analyzed as a function of the W fraction x. It was observed that the optical gap exhibits a nonlinear behavior as a function of x:

$$E_G(x) = (1-x)\,E_G(x=0) + x\,E_G(x=1) - b\,x\,(1-x), \tag{19}$$

with the fitting to DFT calculations yielding a bowing parameter $b = 0.28 \pm 0.04$ eV for A excitons, in good agreement with the experimental value ($b = 0.25 \pm 0.04$ eV). Here $E_G(x=0)$ and $E_G(x=1)$ are the energy gaps of MoS_2 and WS_2, respectively. Specifically, the energy gap of the monolayer alloy $Mo_{1-x}W_xS_2$ deviates from the linear interpolation scheme predicted by the well-known Vegard's law [42,43], corresponding to $b = 0$ in Eq. (19). Therefore, it is established that the energy gap decreases with respect to the MoS_2 value when x is small. This trend qualitatively aligns with the CPA results we obtained for disordered TMDs with binary disorder.

For the purpose of quantitative comparison, we focus on the monolayer alloy $Mo_{1-x}W_xS_2$ across the entire range of W fraction $x \simeq c$ (see Appendix B). In the subsequent CPA calculations, the energy gap appearing in Eq. (1), which describes electrons in the pristine material, is assumed to vary with x in accordance with Vegard's law. Hence

$$\Delta(x) = \tfrac{1}{2}\,(1-x)\,E_G(x=0) + \tfrac{1}{2}\,x\,E_G(x=1), \tag{20}$$

with $E_G(x=0) = 1.791$ eV and $E_G(x=1) = 1.936$ eV, according to the values reported in Ref. [41]. For the sake of simplicity, we adopt a constant valence-band splitting parameter, setting $\alpha = 0.0375$ eV regardless of the W fraction x. While α varies from 0.0375 eV in MoS_2 to 0.1075 eV in WS_2 (see Table I), this premise does not constitute a significant limitation to the accuracy of the results.

Taking all these assumptions into account, the CPA involves only a single fitting parameter, namely, λ_A. The numerical procedure we have followed is, using the bisection method, to find the value of λ_A that reproduces the gap obtained via DFT for $x = 0.5$. We have then used that same value of λ_A to obtain the gap for the remaining values of x using our CPA calculations. In this way, we have found that the value of this parameter that yields the best agreement with the DFT results reported in Ref. [41] is $\lambda_A = 0.46$ eV. Figure 6 displays the energy gap as a function of the W fraction x. We observe that the CPA gap of the alloy deviates significantly from Vegard's law but is in very close agreement with that obtained from DFT. Actually, the resulting bowing parameter $b = 0.284 \pm 0.007$ eV is the same within the uncertainty of the results. Deviation of CPA results from DFT predictions is larger upon increasing x. The CPA overestimation near x approaching unity can be attributed to the larger valence-band splitting parameter α in WS_2 compared to MoS_2. This results in a smaller band gap than that predicted when assuming a constant splitting parameter.

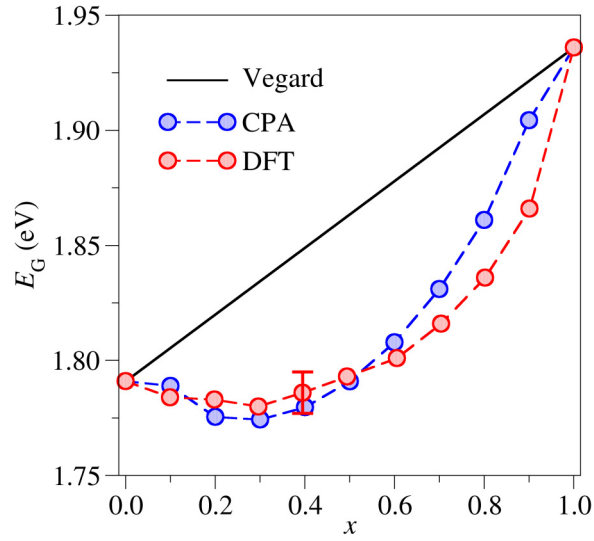

FIG. 6. Energy gap of the alloy $Mo_{1-x}W_xS_2$ as a function of the W fraction x. CPA results when $\lambda_A = 0.46$ eV and $\lambda_B = 0$ (blue circles) are compared to DFT values extracted from Ref. [41] (red circles). The error bar of the DFT value at $x = 0.395$ was obtained after averaging eight configurations of randomly distributed W atoms in the supercell in substitution of Mo atoms, being similar for the other fractions. Dashed lines are a guide to the eye. Black solid line shows the linear interpolation scheme according to Vegard's law.

VI. CONCLUSION

PDs have a significant influence on the electronic states of TMDs, leading to substantial changes in the DOS. DFT calculations are commonly used to quantify these effects, as they offer high accuracy and provide a detailed picture of the local environment around the defect. However, DFT is computationally expensive, which limits the accessible supercell sizes. To overcome these limitations, we have employed the $\boldsymbol{k}\cdot\boldsymbol{p}$ approximation to describe the electronic states in pristine TMDs. Disorder has been modeled as a regular lattice of PDs randomly distributed over a grid. The electron-defect interaction potential has been replaced by a separable pseudopotential, thus allowing us to obtain a solvable model for any arbitrary shape function. Two models of disorder have been considered, namely, binary and Anderson-like. The CPA was employed to calculate the average DOS as a function of disorder strength and an analytic expression for the coupling constant of the effective medium was obtained in the limit of weak Anderson disorder. This method allows for an exact solution of the problem and provides more reliable results than other established approaches, such as the self-consistent Born approximation, particularly in the strong-disorder regime [40]. Notably, both disorder models examined yield consistent results, indicating that increasing disorder strength leads to a reduction in the energy gap. Finally, we compared our results with available DFT data for the optical gap in the monolayer alloy $Mo_{1-x}W_xS_2$. We found that predictions of the binary disorder model are in very good agreement with DFT calculations with only a single fitting parameter,

namely, the strength of the pseudopotential. In our model, the deviation from Vegard's law is attributed to the random distribution of PDs [44], which results in a bowing parameter that shows excellent agreement with both DFT calculations and experimental data. Thus, our model offers the advantage of being computationally less demanding than DFT while still providing results that reasonably match experimental findings.

ACKNOWLEDGMENTS

The authors thank A. Díaz-Fernández for helpful discussions. We acknowledge financial support from Comunidad de Madrid (Recovery, Transformation and Resilience Plan) and NextGenerationEU from the European Union (Grant No. MAD2D-CM-UCM5) and Agencia Estatal de Investigación of Spain (Grant No. PID2022-136285NB-C31/3).

DATA AVAILABILITY

The data that support the findings of this article are not publicly available upon publication because it is not technically feasible and/or the cost of preparing, depositing, and hosting the data would be prohibitive within the terms of this research project. The data are available from the authors upon reasonable request.

APPENDIX A: ONE-BAND APPROXIMATION

The so-called one-band approximation was formerly introduced by Sievert and Glasser to simplify the calculations while retaining accuracy by neglecting interband scattering [37]. Nonetheless, extensions to more intricate situations involving interband scattering have already been proposed [45]. The Green's function operators associated to $\widehat{H}_{\mathrm{M}}$ and $\widehat{H}_0$ in Eq. (7) satisfy [26]

$$\widehat{G}_{\mathrm{M}}(z) = \widehat{G}_0(z) + \widehat{G}_0(z) \sum_n |\omega_n\rangle \lambda \langle \omega_n | \widehat{G}_{\mathrm{M}}(z). \tag{A1}$$

We now take into account the closure relation of the plane waves

$$\sum_{\boldsymbol{k}} |\,\boldsymbol{k}\,\rangle\langle\,\boldsymbol{k}\,| = \mathbb{1}, \tag{A2}$$

where $\mathbb{1}$ is the identity operator and $\langle \boldsymbol{k}|\widehat{G}_0(z)|\boldsymbol{k}'\rangle = G_0(\boldsymbol{k}, z)\,\delta_{\boldsymbol{k},\boldsymbol{k}'}$, with $G_0(\boldsymbol{k}, z) = 1/[z - H_0(\boldsymbol{k})]$, obtaining

$$\langle \boldsymbol{k}|\widehat{G}_{\mathrm{M}}(z)|\boldsymbol{k}'\rangle = G_0(\boldsymbol{k}, z)\delta_{\boldsymbol{k},\boldsymbol{k}'} + \lambda \frac{4\pi^2}{a^2} G_0(\boldsymbol{k}, z)\,\omega(\boldsymbol{k}) \times \sum_{\boldsymbol{K}} \omega^*(\boldsymbol{k}+\boldsymbol{K})\langle \boldsymbol{k}+\boldsymbol{K}|\widehat{G}_{\mathrm{M}}(z)|\boldsymbol{k}'\rangle, \tag{A3}$$

where $\boldsymbol{K}$ runs over the reciprocal vectors of the impurity lattice. In the one-band approximation, the Fourier transform of the shape function is assumed to vanish outside the Brillouin zone [37,45]. In this way, we only retain the term $\boldsymbol{K} = 0$ in the summation appearing in Eq. (A3) since the product $\omega(\boldsymbol{k})\omega^*(\boldsymbol{k}+\boldsymbol{K})$ vanishes otherwise, thereby simplifying the calculations. Therefore,

$$\langle \boldsymbol{k}|\widehat{G}_{\mathrm{M}}(z)|\boldsymbol{k}'\rangle = \mathcal{D}(z, \lambda, \boldsymbol{k})\delta_{\boldsymbol{k},\boldsymbol{k}'}, \tag{A4}$$

where $\mathcal{D}(z, \lambda, \boldsymbol{k})$ is defined in (12c). The translational invariance of the effective medium ensures that the Green's function operator is diagonal in the basis of plane waves. Using the closure relation (A2), we get

$$\langle \omega_n|\widehat{G}_{\mathrm{M}}(z)|\omega_n\rangle = \sum_{\boldsymbol{k}} \langle \boldsymbol{k}|\widehat{G}_{\mathrm{M}}(z)\boldsymbol{k}\rangle |\langle\,\boldsymbol{k}|\omega_n\rangle|^2 = \frac{1}{S}\sum_{\boldsymbol{k}} \langle \boldsymbol{k}|\widehat{G}_{\mathrm{M}}|\boldsymbol{k}\rangle |\omega(\boldsymbol{k})|^2, \tag{A5}$$

where S is the area of the TMD. After converting the sum over $\boldsymbol{k}$ into an integration, we finally obtain (12b).

APPENDIX B: FRACTION OF IMPURITIES

The concentration of W atoms in the monolayer alloy $Mo_{1-x}W_xS_2$ is obtained as $n_{\mathrm{W}} = x/A$, where $A = (\sqrt{3}/2)\,a_{MoS_2}$ and $a_{MoS_2} = 0.31$ nm are the area of the unit cell and the lattice parameter of MoS_2, respectively. In our model of binary disorder, the same concentration is expressed as $n_{\mathrm{W}} = c/a^2$ with $a = 0.3$ nm and, consequently, we can approximate $x \simeq c$ in our calculations.

[1] G. Wang, A. Chernikov, M. M. Glazov, T. F. Heinz, X. Marie, T. Amand, and B. Urbaszek, *Colloquium:* Excitons in atomically thin transition metal dichalcogenides, Rev. Mod. Phys. **90**, 021001 (2018).

[2] T. Chowdhury, E. C. Sadler, and T. J. Kempa, Progress and prospects in transition-metal dichalcogenide research beyond 2D, Chem. Rev. **120**, 12563 (2020).

[3] A. Ahmed, M. Zahir Iqbal, A. Dahshan, S. Aftab, H. H. Hegazy, and E. S. Yousef, Recent advances in 2D transition metal dichalcogenide-based photodetectors: a review, Nanoscale **16**, 2097 (2024).

[4] D. Rhodes, S. H. Chae, R. Ribeiro-Palau, and J. Hone, Disorder in van der Waals heterostructures of 2D materials, Nat. Mater. **18**, 541 (2019).

[5] K. Ko, M. Jang, J. Kwon, and J. Suh, Native point defects in 2D transition metal dichalcogenides: A perspective bridging intrinsic physical properties and device applications, J. Appl. Phys. **135**, 100901 (2024).

[6] G. Moody, C. Kavir Dass, K. Hao, C.-H. Chen, L.-J. Li, A. Singh, K. Tran, G. Clark, X. Xu, G. Berghäuser, E. Malic, A. Knorr, and X. Li, Intrinsic homogeneous linewidth and broadening mechanisms of excitons in monolayer transition metal dichalcogenides, Nat. Commun. **6**, 8315 (2015).

[7] O. A. Ajayi, J. V. Ardelean, G. D. Shepard, J. Wang, A. Antony, T. Taniguchi, K. Watanabe, T. F. Heinz, S. Strauf, X.-Y. Zhu, and J. C. Hone, Approaching the intrinsic photoluminescence linewidth in transition metal dichalcogenide monolayers, 2D Mater. **4**, 031011 (2017).

[8] M. Dwedari, S. Brem, M. Feierabend, and E. Malic, Disorder-induced broadening of excitonic resonances in transition metal dichalcogenides, Phys. Rev. Mater. **3**, 074004 (2019).

[9] Y. Huang and S. Das Sarma, Electronic transport, metal-insulator transition, and Wigner crystallization in transition metal dichalcogenide monolayers, Phys. Rev. B **109**, 245431 (2024).

[10] S.-S. Chee, C. Oh, M. Son, G.-C. Son, H. Jang, T. J. Yoo, S. Lee, W. Lee, J. Y. Hwang, H. Choi, B. H. Lee, and M.-H. Ham, Sulfur vacancy-induced reversible doping of transition metal disulfides *via* hydrazine treatment, Nanoscale **9**, 9333 (2017).

[11] Anne Marie Z. Tan, C. Freysoldt, and R. G. Hennig, Stability of charged sulfur vacancies in 2D and bulk MoS_2 from plane-wave density functional theory with electrostatic corrections, Phys. Rev. Mater. **4**, 064004 (2020).

[12] H. Bretscher, Z. Li, J. Xiao, D. Y. Qiu, S. Refaely-Abramson, J. A. Alexander-Webber, A. Tanoh, Y. Fan, G. Delport, C. A. Williams, S. D. Stranks, S. Hofmann, J. B. Neaton, S. G. Louie, and A. Rao, Rational passivation of sulfur vacancy defects in two-dimensional transition metal dichalcogenides, ACS Nano **15**, 8780 (2021).

[13] D. Vaquero, V. Clericò, J. Salvador-Sánchez, E. Díaz, F. Domínguez-Adame, L. Chico, Y. M. Meziani, E. Diez, and J. Quereda, Fast response photogating in monolayer MoS_2 phototransistors, Nanoscale **13**, 16156 (2021).

[14] J. H. Park, A. Sanne, Y. Guo, M. Amani, K. Zhang, H. C. P. Movva, J. A. Robinson, A. Javey, J. Robertson, S. K. Banerjee, and A. C. Kummel, Defect passivation of transition metal dichalcogenides via a charge transfer van der Waals interface, Sci. Adv. **3**, e1701661 (2017).

[15] J. Y. Kim, Ł. Gelczuk, M. P. Polak, D. Hlushchenko, D. Morgan, R. Kudrawiec, and I. Szlufarska, Experimental and theoretical studies of native deep-level defects in transition metal dichalcogenides, npj 2D Mater. Appl. **6**, 75 (2022).

[16] S. Neupane, H. Tang, and A. Ruzsinszky, Defect-induced states, defect-induced phase transition, and excitonic states in bent tungsten disulfide (WS_2) nanoribbons: Density functional vs. many body theory, Phys. Rev. Mater. **7**, 124001 (2023).

[17] M. F. Hossen, S. Shendokar, and S. Aravamudhan, Defects and defect engineering of two-dimensional transition metal dichalcogenide (2D TMDC) materials, Nanomaterials **14**, 410 (2024).

[18] S. Fang, R. Kuate Defo, S. N. Shirodkar, S. Lieu, G. A. Tritsaris, and E. Kaxiras, *Ab initio* tight-binding Hamiltonian for transition metal dichalcogenides, Phys. Rev. B **92**, 205108 (2015).

[19] J. A. Silva-Guillén, P. San-Jose, and R. Roldán, Electronic band structure of transition metal dichalcogenides from *ab initio* and Slater–Koster tight-binding model, Appl. Sci. **6**, 284 (2016).

[20] M. A. Khan, M. Erementchouk, J. Hendrickson, and M. N. Leuenberger, Electronic and optical properties of vacancy defects in single-layer transition metal dichalcogenides, Phys. Rev. B **95**, 245435 (2017).

[21] M. Aghajanian, A. A. Mostofi, and J. Lischner, Tuning electronic properties of transition-metal dichalcogenides via defect charge, Sci. Rep. **8**, 13611 (2018).

[22] D. Xiao, G.-B. Liu, W. Feng, X. Xu, and W. Yao, Coupled spin and valley physics in monolayers of MoS_2 and other group-VI dichalcogenides, Phys. Rev. Lett. **108**, 196802 (2012).

[23] A. Kormányos, G. Burkard, M. Gmitra, J. Fabian, V. Zólyomi, N. D. Drummond, and V. Fal'ko, $\boldsymbol{k}\cdot\boldsymbol{p}$ theory for two-dimensional transition metal dichalcogenide semiconductors, 2D Mater. **2**, 022001 (2015).

[24] B. T. Zhou, K. Taguchi, Y. Kawaguchi, Y. Tanaka, and K. T. Law, Spin-orbit coupling induced valley Hall effects in transition-metal dichalcogenides, Commun. Phys. **2**, 26 (2019).

[25] A. Gonis, *Green Functions for Ordered and Disordered Systems* (North-Holland, Amsterdam, 1992).

[26] E. N. Economou, *Green's Functions in Quantum Physics* (Springer, Berlin, 2006).

[27] J. Callaway, *Quantum Theory of the Solid State* (Elsevier, Amsterdam, 2013).

[28] M. Lax, Multiple scattering of waves, Rev. Mod. Phys. **23**, 287 (1951).

[29] P. Soven, Coherent-potential model of substitutional disordered alloys, Phys. Rev. **156**, 809 (1967).

[30] B. Velický, S. Kirkpatrick, and H. Ehrenreich, Single-site approximations in the electronic theory of simple binary alloys, Phys. Rev. **175**, 747 (1968).

[31] D. W. Taylor, Vibrational properties of imperfect crystals with large defect concentrations, Phys. Rev. **156**, 1017 (1967).

[32] H. Shiba, A reformulation of the coherent potential approximation and its applications, Prog. Theor. Phys. **46**, 77 (1971).

[33] N. Ito, T. Nomoto, K. Kobayashi, S. Mankovsky, K. Nomura, R. Arita, H. Ebert, and T. Koretsune, Wannier-based implementation of the coherent potential approximation with applications to Fe-based transition metal alloys, Phys. Rev. B **105**, 125136 (2022).

[34] P. W. Anderson, Absence of diffusion in certain random lattices, Phys. Rev. **109**, 1492 (1958).

[35] S. Lebègue and O. Eriksson, Electronic structure of two-dimensional crystals from *ab initio* theory, Phys. Rev. B **79**, 115409 (2009).

[36] Z. Y. Zhu, Y. C. Cheng, and U. Schwingenschlögl, Giant spin-orbit-induced spin splitting in two-dimensional transition-metal dichalcogenide semiconductors, Phys. Rev. B **84**, 153402 (2011).

[37] P. R. Sievert and M. L. Glasser, Interband effects in the coherent-potential approximation. I, Phys. Rev. B **7**, 1265 (1973).

[38] E. de Prunelé, Solvable model for three-dimensional quantum scattering of a particle off several separable interactions centred at n arbitrary points, J. Phys. A: Math. Gen. **30**, 7831 (1997).

[39] C. González-Santander, T. Apostolova, and F. Domínguez-Adame, Binding energy of hydrogenic impurities in quantum dots under intense laser radiation, J. Phys.: Condens. Matter **25**, 335802 (2013).

[40] J. L. Hernando, Y. Baba, E. Díaz, and F. Domínguez-Adame, Many-impurity scattering on the surface of a topological insulator, Sci. Rep. **11**, 5810 (2021).

[41] Y. Chen, J. Xi, D. O. Dumcenco, Z. Liu, K. Suenaga, D. Wang, Z. Shuai, Y.-S. Huang, and L. Xie, Tunable band gap photoluminescence from atomically thin transition-metal dichalcogenide alloys, ACS Nano **7**, 4610 (2013).

[42] L. Vegard, Die Konstitution der Mischkristalle und die Raumfüllung der Atome, Z. Phys. **5**, 17 (1921).

[43] A.-B. Chen and A. Sher, *Semiconductor Alloys* (Springer, New York, 1995).

[44] D. Stroud, Band gaps of semiconductor alloys, Phys. Rev. B **5**, 3366 (1972).

[45] M. L. Glasser and P. R. Sievert, Interband effects in the coherent potential approximation: Simple two band model, Can. J. Phys. **53**, 1109 (1975).